

Mass-loss rates and luminosity functions of dust-enshrouded AGB stars and red supergiants in the LMC

Jacco Th. van Loon¹, M.A.T. Groenewegen³, A. de Koter², Norman R. Trams⁴, L.B.F.M. Waters^{2,5}, Albert A. Zijlstra⁶, Patricia A. Whitelock⁷, Cecile Loup⁸

¹ Institute of Astronomy, Madingley Road, Cambridge CB3 0HA, United Kingdom

² Astronomical Institute, University of Amsterdam, Kruislaan 403, NL-1098 SJ Amsterdam, The Netherlands

³ Max-Planck Institut für Astrophysik, Karl-Schwarzschild Straße 1, D-85740 Garching bei München, Germany

⁴ Astrophysics Division of ESA, ESTEC, P.O.Box 299, NL-2200 AG Noordwijk, The Netherlands

⁵ Space Research Organization Netherlands, Landleven 12, NL-9700 AV Groningen, The Netherlands

⁶ University of Manchester Institute of Science and Technology, P.O.Box 88, Manchester M60 1QD, United Kingdom

⁷ South African Astronomical Observatory, P.O.Box 9, 7935 Observatory, Republic of South Africa

⁸ Institut d'Astrophysique de Paris, 98bis Boulevard Arago, F-75014 Paris, France

Received date; Accepted date

Abstract. A radiative transfer code is used to model the spectral energy distributions of 57 mass-losing Asymptotic Giant Branch (AGB) stars and red supergiants (RSGs) in the Large Magellanic Cloud (LMC) for which ISO spectroscopic and photometric data are available. As a result we derive mass-loss rates and bolometric luminosities.

A gap in the luminosity distribution around $M_{\text{bol}} = -7.5$ mag separates AGB stars from RSGs. The luminosity distributions of optically bright carbon stars, dust-enshrouded carbon stars and dust-enshrouded M-type stars have only little overlap, suggesting that the dust-enshrouded AGB stars are at the very tip of the AGB and will not evolve significantly in luminosity before mass loss ends their AGB evolution.

Derived mass-loss rates span a range from $\dot{M} \sim 10^{-7}$ to $10^{-3} M_{\odot} \text{ yr}^{-1}$. More luminous and cooler stars are found to reach higher mass-loss rates. The highest mass-loss rates exceed the classical limit set by the momentum of the stellar radiation field, L/c , by a factor of a few due to multiple scattering of photons in the circumstellar dust envelope. Mass-loss rates are lower than the mass consumption rate by nuclear burning, \dot{M}_{nuc} , for most of the RSGs. Two RSGs have $\dot{M} \gg \dot{M}_{\text{nuc}}$, however, suggesting that RSGs shed most of their stellar mantles in short phases of intense mass loss. Stars on the thermal pulsing AGB may also experience episodes of intensified mass loss, but their quiescent mass-loss rates are usually already higher than \dot{M}_{nuc} .

Key words: Stars: carbon – circumstellar matter – Stars: mass loss – Stars: AGB and post-AGB – Magellanic Clouds – Infrared: stars

1. Introduction

In their final stages of evolution, both intermediate-mass and more massive stars become very large and assume very low photospheric temperatures. Either as Asymptotic Giant Branch (AGB) stars for initial masses $1 M_{\odot} \lesssim M < M_{\text{up}}$ or as red supergiants (RSGs) for $M > M_{\text{up}}$, with $M_{\text{up}} \sim 8 M_{\odot}$, they become unstable and their mantles start to pulsate with great amplitude. This presumably levitates matter out to a distance from the star where gas temperature and gas density are favourable for the formation of dust. Once dust forms in sufficient abundance, radiation pressure on the dust grains and collisional coupling of the grains with the gas drives an efficient stellar wind (Wickramasinghe et al. 1966; Goldreich & Scoville 1976). In this way, AGB stars and RSGs lose a significant fraction of their initial mass at rates of up to $\dot{M} \sim 10^{-5}$ to $10^{-3} M_{\odot} \text{ yr}^{-1}$, and they become surrounded by a dusty circumstellar envelope (CSE). The stellar light is almost entirely absorbed by the dust at wavelengths $\lambda \lesssim 1 \mu\text{m}$, but re-emission by the dust at $\lambda \gtrsim 10 \mu\text{m}$ makes the CSEs very bright infrared (IR) objects. The dust-enshrouded phase of evolution is particularly interesting for its importance in the chemical enrichment of the interstellar medium (ISM) and the formation of stellar remnants.

IRAS detected many IR point sources in the Large Magellanic Cloud (LMC) (Schwering & Israel 1990), from amongst which a few hundred candidates for CSEs around AGB stars or RSGs could be selected (Reid et al. 1990; Loup et al. 1997, hereafter paper I). Association with known optically bright stars (mostly RSGs) and ground-based near-IR observations have resulted in the identification of several dozen AGB star or RSG counterparts (Reid et al. 1990; Wood et al. 1992; paper I; Zijlstra et al. 1996, hereafter paper II; van Loon et al. 1997, hereafter paper III). Follow-up observations have been pri-

marily done to obtain accurate bolometric luminosities for these stars, which is possible because the distance to the LMC is known with relatively high accuracy, and also, in the case of AGB stars, to determine whether the circumstellar dust and/or the photospheric composition is dominated by an oxygenous or carbonaceous chemistry (van Loon et al. 1998, hereafter paper IV; van Loon et al. 1999a). ISO spectroscopic and photometric observations of a selection of 57 AGB stars and RSGs in the LMC were presented by Trams et al. (1999b), including a thorough chemical classification study. In this paper, the spectral energy distributions (SEDs) of the ISO sample are fitted by a radiation transfer model, yielding mass-loss rates and bolometric luminosities.

The paper is organised as follows: Section 2 describes the input to the model. A number of assumptions have been made for various reasons, either because it is a valid approximation, the parameter is not known, or simply for the sake of restricting the parameter space. The aim has been to maximise homogeneity in modelling our large dataset. Section 3 presents the observed SEDs and their best model fits for all stars in our sample. In Section 4 the resulting bolometric luminosities and mass-loss rates are discussed in detail.

2. Input for the model fitting

2.1. The radiative transfer code

To model the dusty CSE we have used a radiative transfer code (de Koter et al., in preparation). It calculates the emergent SED from a star surrounded by a spherically symmetric dusty CSE. Input parameters include the SED of the underlying star, optical properties of the dust, and parameters describing the CSE geometry. These are discussed below, after a brief description of the observed SEDs.

2.2. Observed spectral energy distributions

The model is fitted to photometric and spectroscopic data in the IR. These data consist of ISO measurements, supplemented by near-IR photometry gathered at the South African Astronomical Observatory (SAAO) within the framework of a monitoring campaign to obtain pulsation periods for the stars in the ISO sample (Whitelock et al. 1999, in preparation). The variability information resulting from the monitoring project will be used for correlation with the results from the model fits. The ISO data comprise broadband photometry at 12, 25 and 60 μm using the ISOCAM and ISOPHOT instruments, and spectroscopy between 2.5 and 12 μm using ISOPHOT and between 7 and 14 μm using ISOCAM. The data are described and presented in detail by Trams et al. (1999b).

Interstellar extinction will be ignored, because the SED will only be studied at wavelengths beyond 1 μm

where interstellar extinction is expected to be insignificant compared to the extinction by the CSE. However, there are indications that along some lines of sight through the LMC this may not be true (paper III). Furthermore, the distance to the stars is assumed to be 50 kpc. Although there is reason to believe that the distance to the LMC may be somewhat larger than this (Feast 1998), the most distance estimates cluster around a value of 50 kpc (Walker 1999).

2.3. Spectral energy distributions in the models

Our sample of stars consist of (oxygen-rich) M-type stars and carbon stars. In Trams et al. (1999b), and references therein, we classified the chemical types of the dusty CSEs of most of the stars in our sample. For the stars for which we do not have spectroscopic information about the stellar photosphere we assume that the chemical composition of the dust corresponds to the carbon or oxygen dominance in the stellar photosphere.

For M stars we use the synthetic spectra published by Fluks et al. (1994) for the wavelength region between 0.1 and 12.5 μm , extended to 1 m by means of a blackbody of the temperature given by Fluks et al. For carbon stars no such data are readily available. Barnbaum et al. (1996) and Lázaro et al. (1994) present spectra of carbon stars at optical (0.4 to 0.7 μm) and near-IR (1 to 4 μm) wavelengths, respectively. From their stars we selected AQ Sgr, an N-type carbon star without infrared excess or strong stellar pulsation, for use as a template.

The effective temperature T_{eff} of the stellar photosphere is only known for a few optically bright stars in our sample where spectral subclasses could be determined, ranging from M1 ($T_{\text{eff}} = 3810$ K) to M10 ($T_{\text{eff}} = 2500$ K). For the oxygen-rich stars without this information we adopt $T_{\text{eff}} = 2890$ K, corresponding to a spectral type M8 III (Fluks et al. 1994). Although cooler than the optically bright stars, this spectral type is more appropriate for the oxygen-rich stars with higher mass-loss rates (see paper IV). For the carbon star (AQ Sgr) we adopt $T_{\text{eff}} = 2804$ K, as measured by means of Lunar occultation techniques (Lázaro et al. 1994). Stellar pulsation, a common feature of mass-losing AGB stars and RSGs, results in an extended atmosphere, and the photospheric spectra for pulsating stars are likely to be affected by this (Bowen 1988; Feast 1996). We ignore not only these possible deviations from the input spectra that we use, but also the variability of T_{eff} during the pulsation cycle. Finally, differences in metallicity may affect the spectral classification and its relation to effective temperature. Though important, it is a poorly explored subject.

2.4. Dust properties

The spectral coverage and resolution of the data do not enable the exact composition and properties of the dust

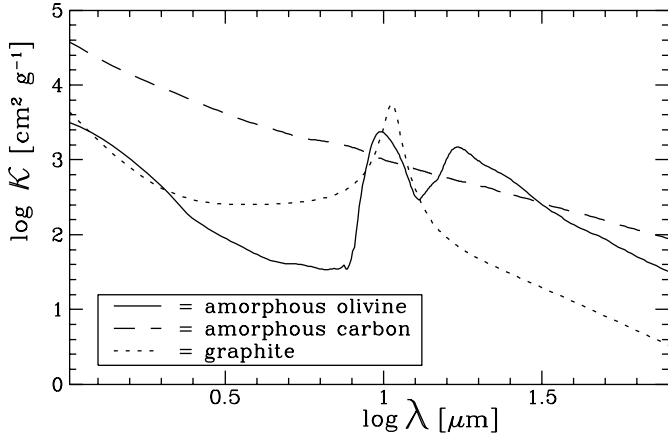


Fig. 1. Opacities for the dust species used: amorphous olivine (solid; Jäger et al. 1998), amorphous carbon (dashed; Preibisch et al. 1993) and graphite (dotted; Laor & Draine 1993).

to be determined. Amorphous olivine and carbon from the Jena group (Jäger et al. 1998; Preibisch et al. 1993) are used for oxygen- and carbon-rich dust, respectively. Crystalline carbon in the form of graphite (SiC), taken from Laor & Draine 1993, is only added when the SiC emission feature at $\sim 11.3 \mu\text{m}$ is observed. The opacities of these three dust species are plotted in Fig. 1. Remaining discrepancies between the best model fit and the observations will be discussed later, and possible explanations include different (mixtures of) dust species. For instance in oxygen-rich environments pyroxenes may contribute, as well as FeO, and in some highly evolved CSEs crystalline silicates may be present (Waters et al. 1999).

The spherical dust grains are assumed all to have the same radius $a = 0.1 \mu\text{m}$, and the optical properties of the grains are calculated assuming Mie theory.

2.5. Geometry of the circumstellar envelope

The dusty CSE has two boundary conditions. The outer boundary is set by insisting that the outer radius of the CSE is at 10^4 stellar radii. This is a rather arbitrary choice, but corresponds roughly to the typical extensions of CSEs. An order of magnitude difference in this ratio does not significantly affect the calculated SED. The inner boundary is set by requiring the temperature at the inner radius, R_{in} , of the dusty CSE to be $T_{\text{dust}} = 1000 \text{ K}$. This corresponds to the typical temperature at which dust condenses, although it should be realised that this depends on the chemistry.

The radiation transfer calculation requires the local density of dust, ρ_{dust} , at a distance r from the center of the star to be specified. The continuity equation for a stationary outflow of a single fluid prescribes

$$\rho_{\text{dust}} = \frac{\dot{M}}{4\pi\psi v_{\text{exp}} r^2} \quad (1)$$

with total (gas+dust) mass-loss rate \dot{M} , gas-to-dust (mass) ratio ψ , and expansion velocity v_{exp} . The parameter that we derive from fitting the model to the observations is \dot{M} . This means that the gas-to-dust ratio is assumed to be known. A value of $\psi = 500$ is adopted here, believed to be representative of the moderately low LMC metallicity. Little is known about the dependence of ψ on the chemical composition of the stellar atmosphere, the effective temperature and the density in the wind at the location of dust condensation. Model calculations for carbon-rich chemistry suggest that ψ decreases with increasing amount of condensible material and increases with increasing T_{eff} (Arndt et al. 1997).

Expansion velocities may be measured from the twin peaks of OH maser profiles, but only a few of the brightest maser sources in the LMC are detectable with current instrumentation (Wood et al. 1986, 1992; paper IV). A value of $v_{\text{exp}} = 10 \text{ km s}^{-1}$ is often adopted for stars in the LMC. However, v_{exp} depends on the stellar luminosity L approximately as $v_{\text{exp}} \propto \sqrt[4]{L}$ (Jura 1984; Habing et al. 1994; see Arndt et al. 1997 for a more detailed approximation). In our modelling we calibrate this scaling relation by demanding a star with $L = 30,000 L_{\odot}$ ($M_{\text{bol}} = -6.47 \text{ mag}$) to have $v_{\text{exp}} = 10 \text{ km s}^{-1}$ (van Loon 1999). Another complication is the fact that dust grains do not escape the stellar gravitation field at a constant velocity. When dust forms in the proximity of the star, matter in the stellar outflow is being accelerated. The velocity v_{exp} as measured by OH is not reached instantaneously. However, dust condensation is not complete instantaneously either, and the two effects tend to cancel: in the dusty CSE the product $\psi(r)v_{\text{exp}}(r)$, which appears in Eq. (1), does not depend on r (e.g. Groenewegen et al. 1998).

The radial optical depth τ_{rad} is the optical depth along the line-of-sight towards the star, and determines the amount of extinction and the temperature structure throughout the dusty CSE. The maximal tangential optical depth τ_{tan} is the optical depth along the line-of-sight parallel to the line-of-sight towards the star, at a minimal distance R_{in} to the star, and measures the amount of emission from the dusty CSE. It is assumed here that $\rho_{\text{dust}} \propto r^{-2}$, i.e. \dot{M} is constant in time. For this simple geometry, with $R_{\text{in}} \ll R_{\text{out}}$, the radial and tangential optical depths are related as

$$\tau_{\text{tan}}/\tau_{\text{rad}} = \pi \quad (2)$$

When presenting the results of the model fits, the values of τ_{rad} at a wavelength $\lambda = 1 \mu\text{m}$ are listed.

2.6. Fitting strategy

The strategy to obtain the best fit of the model to the observations involves iterations of model calculations where input parameters are being adjusted according to the following (rough) guidelines: (i) adjust R_{\star} to reproduce L ; (ii) adjust \dot{M} to fit the $25 \mu\text{m}$ flux density; (iii) adjust

Table 1. Model parameters for M-type stars with ISO spectra, using amorphous olivine from Jena. For a given star, R_\star (in R_\odot), R_{in} (in R_\star), and τ_{rad} (at a wavelength $\lambda = 1\mu\text{m}$) are adjusted to fit the model to the observations, yielding \dot{M} (in $10^{-6} M_\odot \text{ yr}^{-1}$). Model fits derived for multiple epochs are labelled in the last column.

Star	T_{eff}	R_\star	R_{in}	τ_{rad}	\dot{M}	Ep.
HV12070	3309	600	11.2	0.021	0.5	
HV2446	3434	540	13.3	0.054	1.5	
HV888	3574	1300	15.5	0.041	5	
HV996	3574	950	16.5	0.16	13	
IRAS04545–7000	2890	850	12.0	7.1	280	
IRAS05003–6712	2890	560	9.5	1.7	29	
IRAS05298–6957	2890	400	13.0	14	230	A
	2890	800	12.0	7.5	230	B
IRAS05329–6708	2890	600	12.0	7.7	180	
IRAS05402–6956	2890	850	11.5	5.1	180	A
	2890	550	12.0	7.6	180	B
IRAS05558–7000	2890	750	9.8	2.1	50	A
	2890	480	10.5	3.0	50	B
SP77 30–6	2890	700	8.0	0.35	7	
WOH G64	3126	2100	16.0	12	2800	

Table 2. Model parameters for M-type stars without ISO spectra, using amorphous olivine from Jena. For a given star, R_\star (in R_\odot), R_{in} (in R_\star), and τ_{rad} (at a wavelength $\lambda = 1\mu\text{m}$) are adjusted to fit the model to the observations, yielding \dot{M} (in $10^{-6} M_\odot \text{ yr}^{-1}$).

Star	T_{eff}	R_\star	R_{in}	τ_{rad}	\dot{M}
HV12501	3810	840	19.7	0.034	3
HV2360	3736	870	19.2	0.083	7
HV5870	3434	820	13.6	0.10	5
HV916	3666	1050	17.5	0.060	6
IRAS04407–7000	2890	1150	8.9	1.1	50
IRAS04498–6842	2890	770	8.9	1.0	26
IRAS04509–6922	2500	950	6.0	0.83	17
IRAS04516–6902	2667	1200	7.0	0.93	33
IRAS04530–6916	2890	1400	12.5	9.5	840
IRAS05294–7104	2890	800	9.9	2.1	64
SHV0522023–701242	3666	160	16.7	0.001	$\lesssim 0.01$
SHV0524565–694559	3434	190	13.1	0.034	0.2
SHV0530323–702216	3309	280	11.3	0.053	0.4
WOH SG374	3309	730	13.0	0.59	23

R_{inner} to fit the extinction in the near-IR. The aim is to reach $T_{\text{dust}} = 1000 \text{ K}$ at R_{in} , where T_{dust} refers to the hottest component in the case of a mixture of dust species. If a spectrum around $10 \mu\text{m}$ is available, then the strength of the silicate (or SiC) feature and the level of the stellar and/or dust continuum are additional criteria to be met. First $v_{\text{exp}} = 10 \text{ km s}^{-1}$ is used, but afterwards v_{exp} and \dot{M} are scaled as described in Section 2.5, using L from the final fit of the model to the observations. The resulting values for L and \dot{M} — as opposed to R_{inner} — are rather

Table 3. Model parameters for carbon stars with ISO spectra (assuming type C5 with $T_{\text{eff}} = 2804 \text{ K}$), using amorphous carbon from Jena and crystalline carbon (SiC) from Laor & Draine (1993). For a given star, R_\star (in R_\odot), R_{in} (in R_\star), the mass fraction (in %) of dust contained into SiC, and τ_{rad} (at a wavelength $\lambda = 1\mu\text{m}$) are adjusted to fit the model to the observations, yielding \dot{M} (in $10^{-6} M_\odot \text{ yr}^{-1}$). Model fits derived for multiple epochs are labelled in the last column.

Star	R_\star	R_{in}	SiC	τ_{rad}	\dot{M}	Ep.
HV2379	330	9.5	0	1.4	0.6	A
	270	9.6	0	1.7	0.6	B
IRAS04374–6831	480	10.6	0	7.4	8	
IRAS05112–6755	580	10.8	0	11	14	
IRAS05128–6455	600	10.3	0	5.0	6	
IRAS05190–6748	520	11.0	0	17	19	
IRAS05289–6617	290	12.6	20	67	41	A
	220	13.3	20	84	41	B
IRAS05348–7024	650	11.1	50	12	26	A
	500	11.3	50	9.2	26	B
IRAS05568–6753	450	12.2	0	56	55	
SHV0500193–681706	340	10.0	0	2.2	1.9	A
	500	9.8	0	3.2	1.9	B
SHV0500233–682914	480	9.7	20	1.5	1.6	

insensitive to the exact value of T_{eff} , which for many of our stars is not known from observations.

3. Results of model fitting

The results of the model fits are listed in Tables 1 to 5, and the model SEDs are presented together with the observational data in Figs. 2 to 6. The stars are discussed in separate sections according to the chemistry and the availability of ISO spectroscopy. The peculiar carbon star IRAS04496–6958 is described in a section of its own. When more than one epoch of data was available, both epochs were fitted with the requirement that the mass-loss rate remains the same. The approach taken here is not entirely correct, as the stars are all Long Period Variables requiring dynamical models (Hron et al. 1998).

3.1. M-type stars with ISO spectra

The input spectral types and model fit parameters for the M-type stars for which we have ISO spectroscopic data are listed in Table 1, and the model fits are plotted together with the photometric and spectroscopic data in Fig. 2.

Examples of good fits are IRAS05329–6708 and SP77 30–6, for which both the general shape of the SED and the shape and strength of the $10 \mu\text{m}$ silicate feature are well reproduced by the model. The only serious flaw in the fit for these stars is the discrepancy between the observed and predicted $60 \mu\text{m}$ flux density. This is seen in all fits, without exception, including carbon stars. The data do not reveal any trend with luminosity, mass-loss rate or

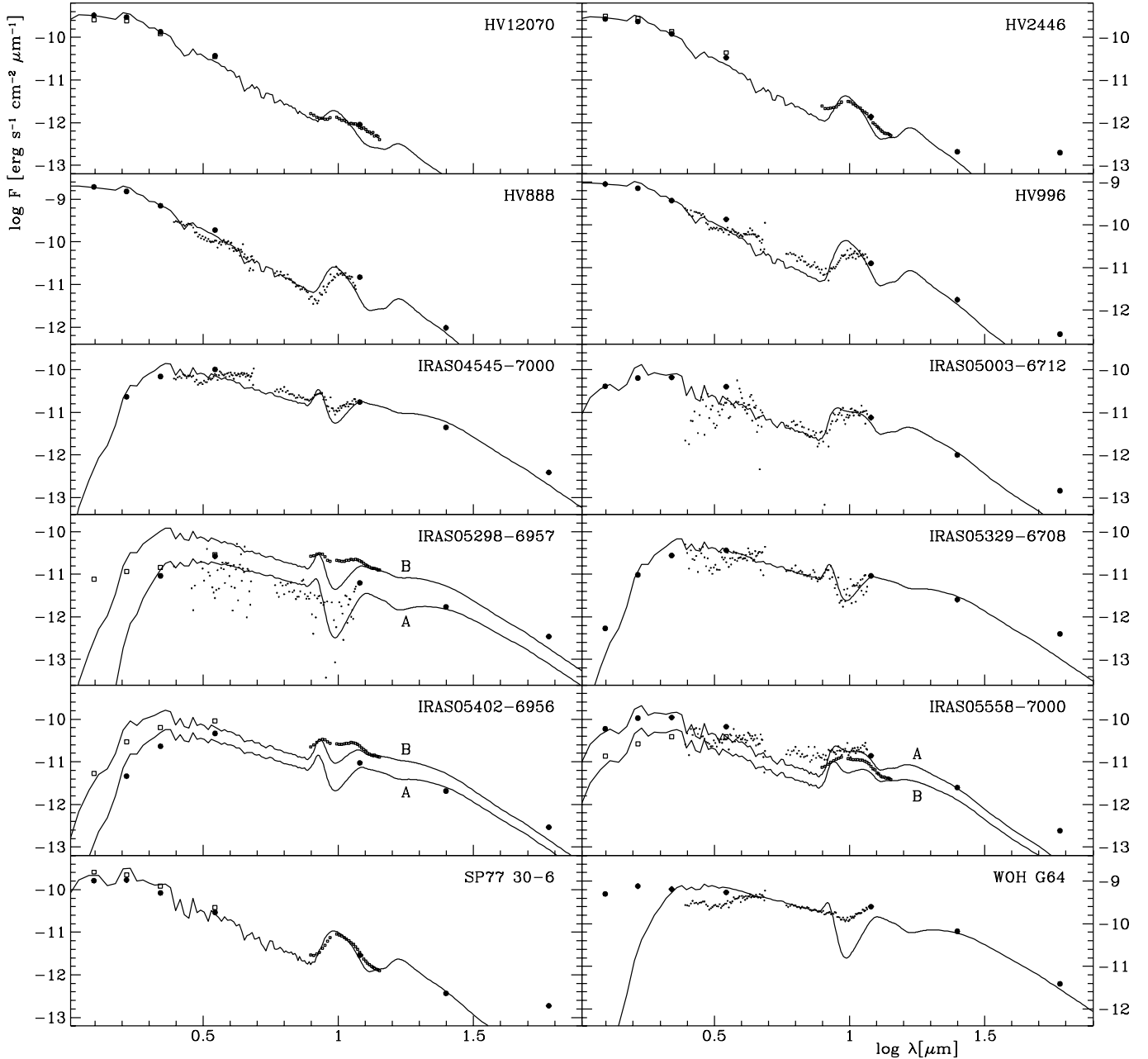


Fig. 2. Model fits (solid lines, Table 1) and observational data (solid circles for epoch A and open squares for epoch B) for M-type stars with ISO spectra.

IR colour, nor with the time that a dust particle spends in the dust shell, $t = 10^4 R_\star / V_{\text{exp}}$, or the density at the inner radius of the dust shell, $\rho = \dot{M} / 4\pi R_{\text{in}}^2 v_{\text{exp}}$. There are three possible explanations: (i) the measured $60 \mu\text{m}$ flux densities may have been over-estimated (Trams et al. 1999b); (ii) a contribution of large ($a \gtrsim 1 \mu\text{m}$) and/or cool ($T \lesssim 200 \text{ K}$) grains would enhance the emission at far-IR wavelengths, in which case a trend of increasing $F_{\text{observed}}/F_{\text{model}} [60 \mu\text{m}]$ for larger t or ρ is expected. This cannot be confirmed with the current dataset, but the quality of the $60 \mu\text{m}$ data is not high enough to rule it out

either; (iii) a shallower slope of the SED at far-IR wavelengths may be obtained by increasing the complex term of the optical constants, thereby increasing the emission in the far-IR over the extinction at shorter wavelengths.

Often the silicate feature produced by the model using amorphous olivine is too strong compared to that observed, i.e. for HV996 and IRAS05402-6956. For HV12070 this may be due to the fact that it is an MS-type star, i.e. a star with a carbon-to-oxygen ratio smaller than but close to 1, and hence the dust may be of a rather peculiar chemical composition. The observed silicate emis-

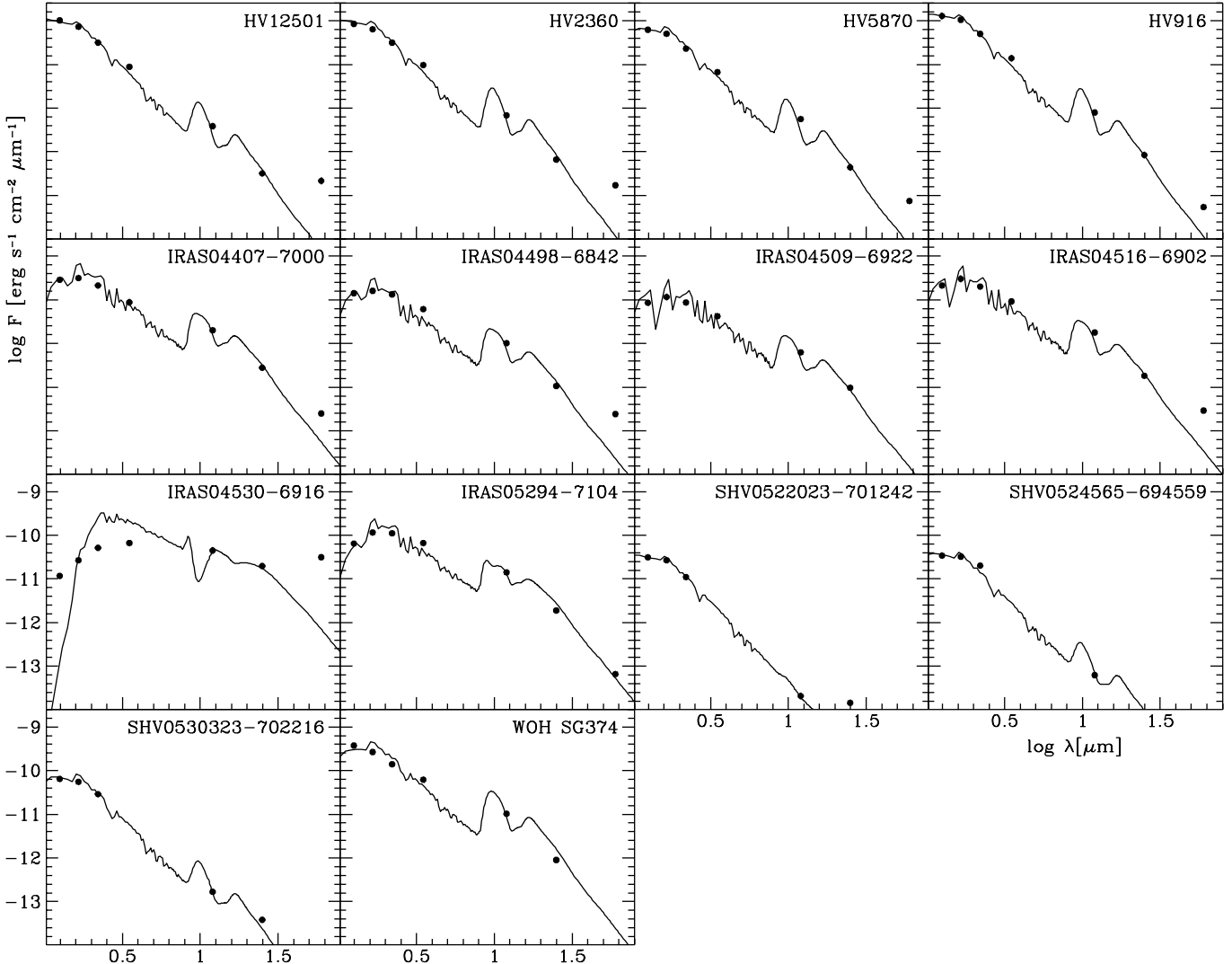


Fig. 3. Model fits (solid lines, Table 2) and observational data for M-type stars without ISO spectra.

sion sometimes peaks at a longer wavelength than does the model, which may be caused by our assumption of spherical grain shape: a continuous distribution of ellipsoids would yield somewhat broader emission features at a wavelength that can be a few $0.1 \mu\text{m}$ longer. Perhaps the silicate dust in the LMC is different from silicate dust that is formed at solar metallicity.

A third discrepancy seen for some, but not all, stars is an emission deficiency in the model fit in the wavelength interval between ~ 4 and $8 \mu\text{m}$, i.e. for HV996 and IRAS05558–7000. This is known from the literature to be a common problem in fitting models to oxygen-rich CSEs, and it is investigated in detail for the post-AGB star AFGL4106 by Molster et al. (1999). Possible explanations include small, hot grains, or a different chemical composition of the dust.

The two stars for which we had most difficulties in reaching an acceptable fit are IRAS05298–6957 and WOH G64. The common problem is reproducing the observed

weak extinction in the near-IR and the silicate feature compared to the strong mid- and far-IR emission. One possible explanation is that of a disk-like shape of the CSE, in which case the disks of these stars are viewed under a large inclination angle causing little extinction in the line-of-sight towards the stars. Perhaps we see here the progenitors of the disk-like and bipolar morphologies common for planetary nebulae and post-RSGs. Alternatively, their dusty CSEs may be clumpy (see e.g. the recent spatially resolved observations of IRC+10216 by Weigelt et al. 1998 and AFGL 4106 by van Loon et al. 1999b).

3.2. M-type stars without ISO spectra

The input spectral types and model fit parameters for the M-type stars for which we do not have ISO spectroscopic data are listed in Table 2, and the model fits are plotted together with the photometric data in Fig. 3.

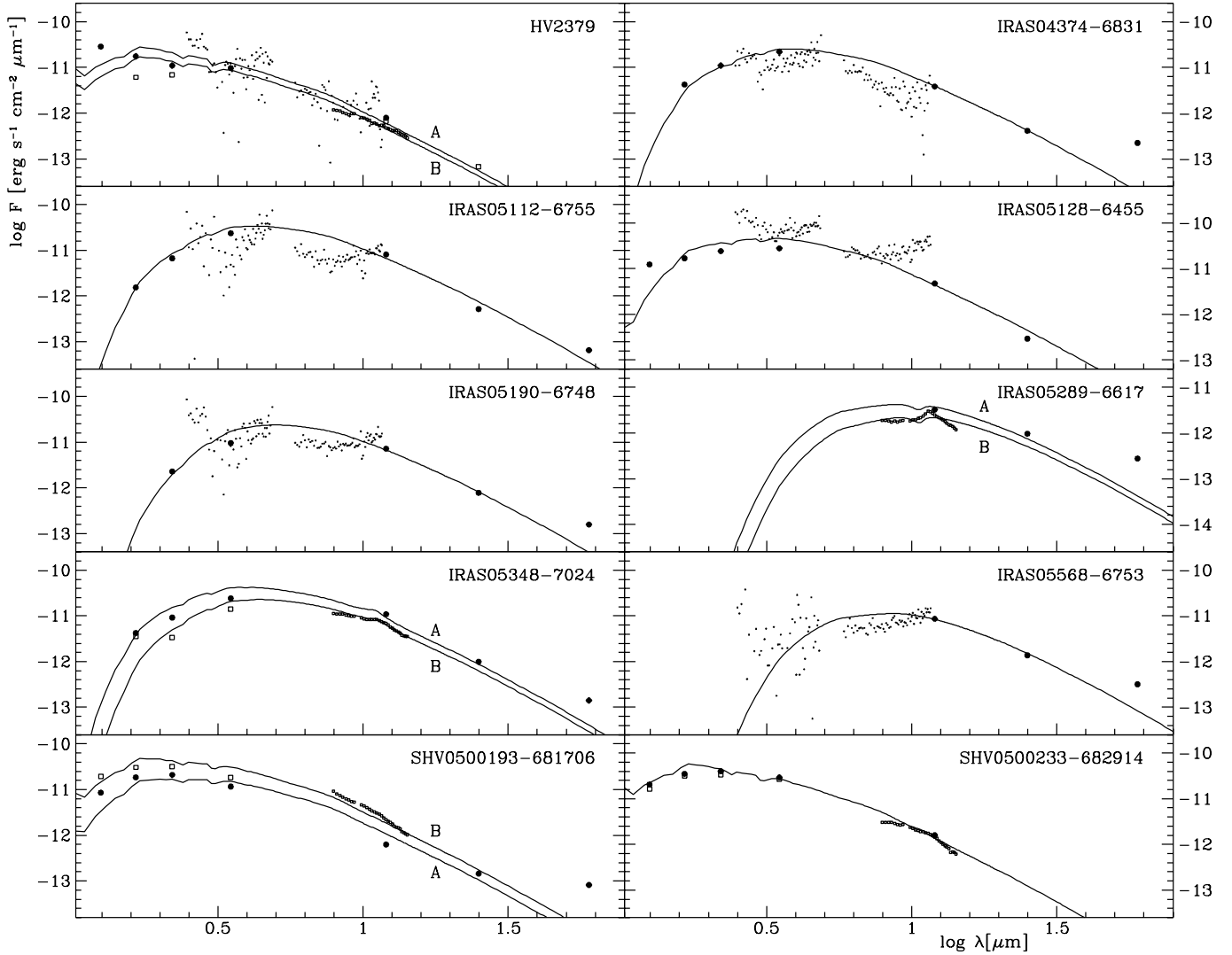


Fig. 4. Model fits (solid lines, Table 3) and observational data (solid circles for epoch A and open squares for epoch B) for carbon stars with ISO spectra.

In general, good fits of the model to the observed SEDs are obtained, disregarding the $60\ \mu\text{m}$ flux densities. This is likely connected to the fact that there is no information about the strength of the silicate feature or the emission between 4 and $8\ \mu\text{m}$. IRAS04530–6916 may well be an example of a star like WOH G64, for which we argued that the CSE may be disk-like.

The only M-type star that has an SED consistent with no mass loss is SHV0522023–701242 (the ISOPHOT measurement at $25\ \mu\text{m}$ for this star is consistent with no detection), indicating that we are able to detect mass-loss rates in excess of a few $\times 10^{-8}\ M_{\odot}\ \text{yr}^{-1}$.

3.3. Carbon stars with ISO spectra

The model fit parameters for the carbon stars for which we have ISO spectroscopic data are listed in Table 3, and

the model fits are plotted together with the photometric and spectroscopic data in Fig. 4.

The general shape of the SED can be reproduced by the model rather well, but in several cases the observed spectra lack emission in the wavelength interval between ~ 5 and $10\ \mu\text{m}$. This may be attributed to the absorption by carbonaceous molecules (Hron et al. 1998). The discrepancy between the ISO spectrum and the photometric data of IRAS05128–6455 may be related to a problem in the background subtraction of the PHOT-S spectrum.

The strength of the silicon carbide (SiC) feature in the spectrum of IRAS05348–7024 could be well reproduced by a mixture of equal quantities of amorphous carbon and crystalline SiC. This would imply a very high crystalline dust content. The SiC fractions are sensitive to the optical constants used — which may be metallicity dependent — and to possible differences in the geometrical distributions of the dust species. Such flaws in our modelling might also

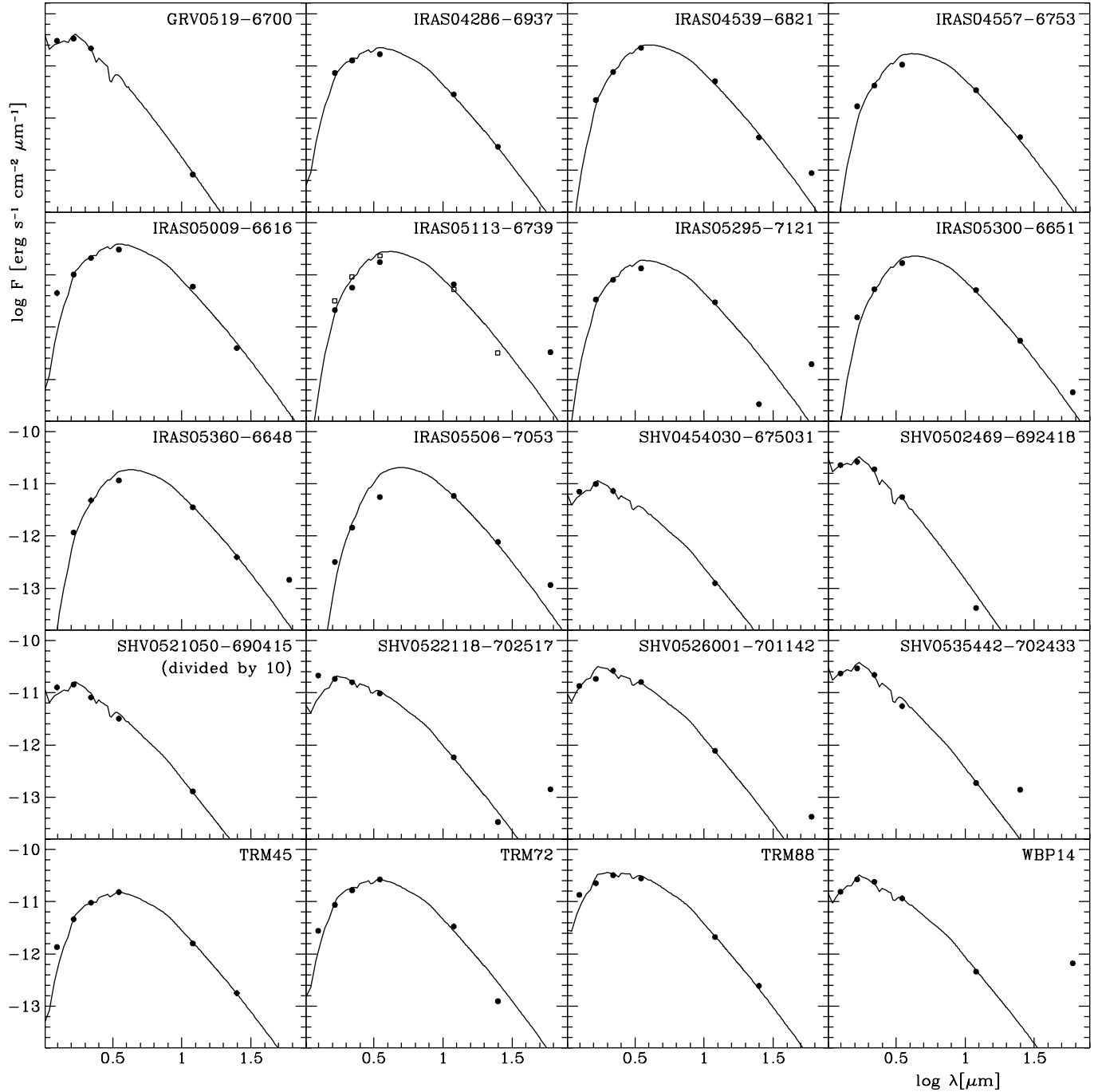


Fig. 5. Model fits (solid lines, Table 4) and observational data (solid circles for epoch A and open squares for epoch B) for carbon stars without ISO spectra. The 12 and 25 μm flux densities of IRAS05506–7053 are IRAS data (Trams et al. 1999b).

explain the problem in reproducing the SiC feature in the very obscured object IRAS05289–6617.

3.4. Carbon stars without ISO spectra

The model fit parameters for the carbon stars for which we do not have ISO spectroscopic data are listed in Table 4, and the model fits are plotted together with the

photometric data in Fig. 5. The ISOPHOT photometry of IRAS05506–7053 may have been in error, the 12 and 25 μm flux densities being consistent with no detection whilst even without an IR excess this star should have been detected easily. Adopting the IRAS photometry the SED may be (poorly) fitted using amorphous carbon instead of silicates. Hence we have reclassified this star as a

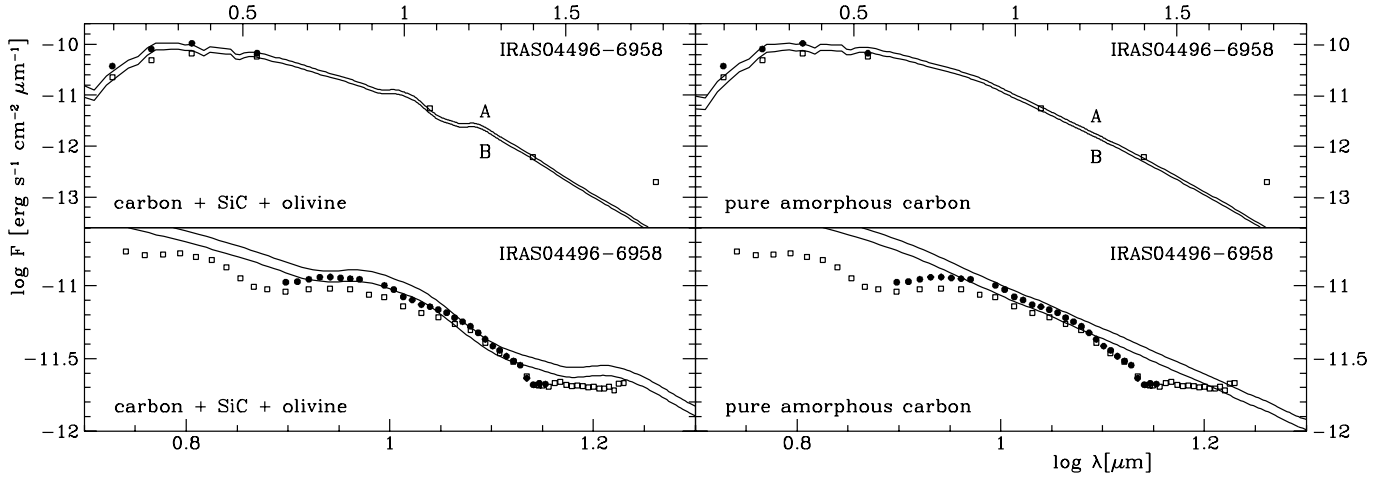


Fig. 6. Model fit to the observed spectral energy distribution of the peculiar carbon star IRAS04496–6958 (Table 5), using a mixture of amorphous carbon, silicon carbide and amorphous olivine (left), and using pure amorphous carbon (right).

Table 4. Model parameters for carbon stars without ISO spectra (assuming type C5 with $T_{\text{eff}} = 2804$ K), using amorphous carbon from Jena. For a given star, R_* (in R_{\odot}), R_{in} (in R_*), and τ_{rad} (at a wavelength $\lambda = 1\mu\text{m}$) are adjusted to fit the model to the observations.

Star	R_*	R_{in}	τ_{rad}	\dot{M}
GRV0519–6700	320	8.5	0.016	$\lesssim 0.01$
IRAS04286–6937	430	10.4	6.4	5
IRAS04539–6821	490	10.7	10	10
IRAS04557–6753	410	10.8	11	8
IRAS05009–6616	570	10.4	6.7	8
IRAS05113–6739	520	10.8	10	11
IRAS05295–7121	410	10.6	8.1	6
IRAS05300–6651	480	10.8	12	11
IRAS05360–6648	430	10.8	11	9
IRAS05506–7053	480	11.0	17	16
SHV0454030–675031	190	9.2	0.76	0.15
SHV0502469–692418	290	8.5	0.018	$\lesssim 0.01$
SHV0521050–690415	680	8.9	0.44	0.6
SHV0522118–702517	300	9.6	1.7	0.7
SHV0526001–701142	360	9.5	1.5	0.8
SHV0535442–702433	320	8.8	0.23	0.1
TRM45	350	10.4	6.0	3.5
TRM72	460	10.3	5.6	5
TRM88	490	10.0	3.1	3
WBP14	330	9.3	1.0	0.5

carbon star, superseding the result obtained by Trams et al. (1999b).

All SEDs can be fit satisfactorily, disregarding the 60 μm flux densities. The ISOPHOT measurement at 25 μm of IRAS05295–7121, which is at a very faint level indeed, bears a large uncertainty and is within the errorbars consistent with the model fit.

Two stars, GRV0519–6700 and SHV0502469–692418, have SEDs consistent with no mass loss: like for oxygen-

Table 5. Model parameters for the silicate carbon star IRAS04496–6958, assuming spectral type C5 with $T_{\text{eff}} = 2804$ K, and using amorphous carbon and olivine from Jena and crystalline carbon (SiC) from Laor & Draine (1993). R_* (in R_{\odot}), R_{in} (in R_*), the mass fraction (in %) of dust contained into SiC and olivine, respectively, and τ_{rad} (at a wavelength $\lambda = 1\mu\text{m}$) are adjusted to fit the model to the observations, yielding \dot{M} (in $10^{-6} M_{\odot} \text{yr}^{-1}$). Model fits derived for multiple epochs are labelled in the last column

Model	R_*	R_{in}	SiC	olivine	τ_{rad}	\dot{M}	Ep.
Sil.+carbon	760	10.0	10	60	2.4	12	A
	680	10.1	10	60	2.6	12	B
Carbon	820	9.9	0	0	3.0	5.6	A
	730	10.1	0	0	3.3	5.6	B

rich CSEs, mass-loss rates in excess of a few $\times 10^{-8} M_{\odot} \text{yr}^{-1}$ are detectable in our data.

3.5. IRAS04496–6958

The ISO data of this star have been discussed extensively in Trams et al. (1999a), where the authors argue for the presence of a minor fraction of silicate dust in the CSE.

Here we fit the SED of this silicate carbon star with a dust mixture of amorphous carbon, olivine and SiC, and also using pure amorphous carbon dust. The model fit parameters for the carbon star IRAS04496–6958 are listed in Table 5, and the model fits are plotted together with the photometric and spectroscopic data in Fig. 6.

Because of the smaller opacity of olivine, the mixture requires lower luminosities and higher mass-loss rates in order to fit the observed SED than in the case of pure carbon only. The shape of the SED around 10 μm is partly

Table 6. Bolometric magnitudes M_{bol} , absolute K-band magnitudes M_K , $(K - L)$ colours and bolometric corrections BC_K relative to M_K of the M-type stars. The distance to the LMC is assumed $d = 50$ kpc, and the bolometric magnitude of the Sun $M_{\text{bol},\odot} = -4.72$.

Star	M_{bol}	M_K	$(K - L)$	BC_K
HV12070	-6.75	-9.75	0.47	3.00
HV12501	-8.09	-10.74	0.45	2.65
HV2360	-8.09	-10.74	0.55	2.65
HV2446	-6.69	-9.75	0.53	3.06
HV5870	-7.60	-10.39	0.50	2.79
HV888	-8.77	-11.60	0.43	2.83
HV916	-8.42	-11.24	0.45	2.82
HV996	-8.09	-10.91	0.75	2.82
IRAS04407-7000	-7.52	-10.31	0.88	2.79
IRAS04498-6842	-6.65	-9.79	1.00	3.14
IRAS04509-6922	-6.42	-9.34	1.05	2.92
IRAS04516-6902	-7.22	-10.25	1.01	3.03
IRAS04530-6916	-7.93	-8.76	2.13	0.83
IRAS04545-7000	-6.85	-9.09	2.25	2.24
IRAS05003-6712	-5.95	-9.04	1.30	3.09
IRAS05294-7104	-6.72	-9.59	1.30	2.87
IRAS05298-6957	-5.21	-6.89	3.00	1.68
	-6.72	-7.39	2.60	0.67
IRAS05329-6708	-6.09	-8.09	2.15	2.00
IRAS05402-6956	-5.90	-7.89	2.60	1.99
	-6.85	-8.99	2.25	2.14
IRAS05558-7000	-6.58	-9.59	1.30	3.01
	-5.61	-8.46	1.83	2.85
SHV0522023-701242	-4.33	-7.09	2.76	2.76
SHV0524565-694559	-4.42	-7.74	3.32	3.32
SHV0530323-702216	-5.10	-8.14	3.04	3.04
SP77 30-6	-6.45	-9.49	0.65	3.04
WOH G64	-9.19	-11.51	1.66	2.32
WOH SG374	-7.17	-9.85	0.95	2.68

reproduced using the mixture, featuring emission from olivine at ~ 10 and $18\mu\text{m}$, and from SiC at $\sim 11.5\mu\text{m}$. The oxygen-rich dust component is likely to be in a stationary disk configuration rather than evenly distributed in the spherically symmetric, outflowing CSE (Trams et al. 1999a). This may be the cause for the very high estimate of the olivine fraction of 60%, which disagrees with the observed IR colours that are entirely dominated by carbon-rich dust. Hence we adopt instead the luminosity and mass-loss rate derived when using pure carbon. The model fit using pure carbon would imply strong molecular absorption in the 5 to 9 μm region and around 14 μm (see also Hron et al. 1998).

4. Discussion

4.1. Luminosities

Luminosities derived from the model fits are listed for M-type and carbon stars in Tables 6 & 7, respectively, together with $(K - L)$ colours and bolometric corrections

Table 7. Bolometric magnitudes M_{bol} , absolute K-band magnitudes M_K , $(K - L)$ colours, and bolometric corrections BC_K relative to M_K of the carbon stars. The distance to the LMC is assumed $d = 50$ kpc, and the bolometric magnitude of the Sun $M_{\text{bol},\odot} = -4.72$.

Star	M_{bol}	M_K	$(K - L)$	BC_K
GRV0519-6700	-4.68	-7.82		3.14
HV2379	-4.73	-7.09	1.70	2.36
	-4.29	-6.59		2.30
IRAS04286-6937	-5.30	-7.24	2.15	1.96
IRAS04374-6831	-5.54	-7.09	2.55	1.55
IRAS04496-6958	-6.70	-9.54	1.35	2.84
	-6.45	-9.04	1.60	2.59
IRAS04539-6821	-5.59	-6.69	3.00	1.00
IRAS04557-6753	-5.20	-6.04	2.85	0.84
IRAS05009-6616	-5.92	-7.79	2.25	1.87
IRAS05112-6755	-5.96	-6.54	3.22	0.58
IRAS05113-6739	-5.72	-6.63	2.96	0.91
IRAS05128-6455	-6.03	-7.94	2.00	1.91
IRAS05190-6748	-5.72	-5.39	3.40	-0.33
IRAS05289-6617	-4.45			
	-3.84			
IRAS05295-7121	-5.20	-6.74	2.40	1.54
IRAS05300-6651	-5.54	-6.29	3.10	0.75
IRAS05348-7024	-6.20	-6.89	2.90	0.69
	-5.63	-5.79	3.40	0.16
IRAS05360-6648	-5.31	-6.19	2.80	0.88
IRAS05506-7053	-5.54	-4.89	3.30	1.35
IRAS05568-6753	-5.40			
SHV0454030-675031	-3.53	-6.64		3.11
SHV0500193-681706	-4.79	-7.79	1.20	3.00
	-5.63	-8.24	1.25	2.61
SHV0500233-682914	-5.54	-8.39	1.55	2.85
SHV0502469-692418	-4.46	-7.68	0.51	3.22
SHV0521050-690415	-6.30	-9.26	0.83	2.96
SHV0522118-702517	-4.52	-7.49	1.30	2.97
SHV0526001-701142	-4.92	-8.04	1.30	3.12
SHV0535442-702433	-4.67	-7.84	0.35	3.17
TRM45	-4.86	-6.94	2.05	2.08
TRM72	-5.45	-7.53	2.36	2.08
TRM88	-5.59	-8.25	1.69	2.66
WBP14	-4.73	-7.94	1.05	3.21

BC_K relative to the K-band magnitudes. In Fig. 7 these bolometric corrections are plotted against the $(K - L)$ colours. The carbon stars define a rather tight relation of the form

$$BC_K = 3 - (K - L)^3/12 \quad (3)$$

valid for $0 < (K - L) < 4$ mag. Bolometric magnitudes can be estimated for obscured stars in this colour interval with an accuracy of a few $\times 0.1$ mag. If the scatter in the data is due to limited accuracies of the photometry and/or model fitting, then luminosities can be estimated with help of the mean relationship to an accuracy of perhaps only ~ 0.1 mag. M-type stars obey approximately the same relation between BC_K and $(K - L)$ as carbon stars do,

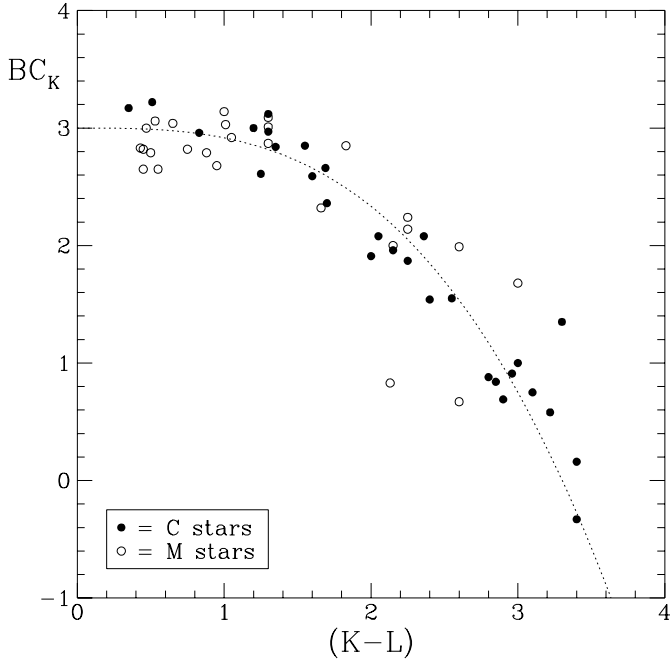


Fig. 7. Bolometric corrections BC_K relative to the K-band magnitudes, versus $(K - L)$ colours. The relation is virtually identical for carbon and M-type stars, and is well represented by the function given in Eq. (3) (dotted line).

although the scatter in the M-type stars seems larger and they appear to have BC_K smaller by $\sim 0.19 \pm 0.09$ mag for $(K - L) < 1$ mag.

The bolometric luminosity distributions of the carbon and M-type stars are plotted in Fig. 8. The distributions resemble those presented in van Loon et al. (1999a). Only stars with $\dot{M} \geq 10^{-7} M_{\odot} \text{ yr}^{-1}$ are plotted, together with the optically bright carbon stars in the LMC from Costa & Frogel (1996). Optically bright carbon stars, dust-enshrouded carbon stars, and dust-enshrouded M-type AGB stars and RSGs occupy distinct luminosity ranges with little overlap: optically bright carbon stars populate the AGB mostly between $M_{\text{bol}} = -4$ and -5 mag, whilst most dust-enshrouded carbon stars have luminosities between $M_{\text{bol}} = -5$ and -6 mag. M-type AGB stars are mainly found between $M_{\text{bol}} = -6$ and -7 mag, and (M-type) RSGs peak around $M_{\text{bol}} = -8$ mag.

Carbon stars result from the dredge-up of carbon during thermal pulses. The fact that the dust-enshrouded carbon stars are more luminous than the optically bright carbon stars suggests that (i) mass-loss rates increase during the thermal-pulsing AGB (TP-AGB) rendering carbon stars optically invisible before they leave the AGB and/or (ii) carbon stars with more massive cores spend a larger fraction of their TP-AGB lifetime being obscured by a massive CSE than carbon stars with less massive cores. If (i) is true then dust-enshrouded carbon stars are closer to the tip of the AGB than are their optically visible coun-

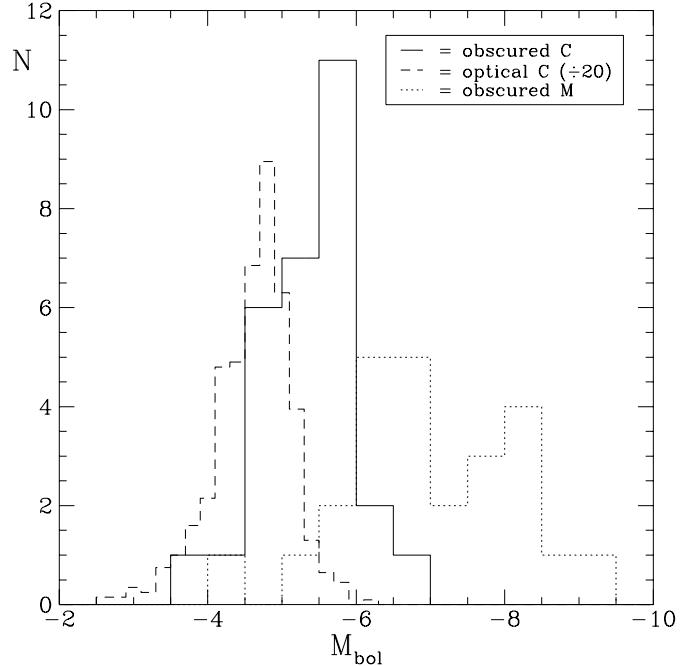


Fig. 8. Bolometric luminosity distribution of carbon and M-type stars with $\dot{M} \geq 10^{-7} M_{\odot} \text{ yr}^{-1}$, compared to the optically bright carbon stars in the LMC (divided by 20) from Costa & Frogel (1996). The luminosity distribution of dust-enshrouded carbon stars peaks at a luminosity higher than optically bright carbon stars, but lower than dust-enshrouded M-type stars. RSGs and AGB stars are separated by a gap in the luminosity distribution around $M_{\text{bol}} \sim -7.5$ mag.

terparts, in which case their luminosity distribution (Fig. 8) will be representative of the progenitors of Planetary Nebulae. This is also valid for the M-type AGB stars that do not seem to evolve much in luminosity once they have become dust-enshrouded: if their luminosities would still increase by more than a factor of two then many more dust-enshrouded M-type AGB stars would be expected with $M_{\text{bol}} < -6$ mag.

Among the dust-enshrouded AGB stars, the luminosity distribution of M-type stars peaks at $M_{\text{bol}} \sim -6.5$ mag which is significantly more luminous than the peak of the carbon star luminosity distribution at $M_{\text{bol}} \sim -5.7$ mag. If, as suggested above, luminosities of dust-enshrouded AGB stars can be directly translated into progenitor masses then the division of $M_{\text{bol}} \sim -6.0$ mag between the dust-enshrouded M-type and carbon star luminosity distributions translates to a Zero Age Main Sequence (ZAMS) mass of $M_{\text{div}} \sim 4 M_{\odot}$ (Wood 1998). Stars with $M_{\text{ZAMS}} < M_{\text{div}}$ become carbon stars on the TP-AGB. Our sample of dust-enshrouded carbon stars contains stars as faint as $M_{\text{bol}} \sim -4$ mag, implying a lower limit to the progenitor mass of carbon stars between 1 and $2 M_{\odot}$ (Wood 1998). This lower mass limit should be regarded as tentative, because the way our sample was selected will result

in faint dust-enshrouded stars being under-represented. It is in good agreement, though, with the $1.5 M_{\odot}$ lower limit to carbon star formation as estimated by Groenewegen & de Jong (1993).

Stars with $M_{ZAMS} > M_{div}$ stay oxygen rich on the TP-AGB. This is expected if Hot Bottom Burning (HBB; Iben 1981; Iben & Renzini 1983; Wood et al. 1983) is effective: in sufficiently massive stars the pressure and temperature at the bottom of the convective mantle are high enough for carbon to be processed into (mainly) nitrogen, thus preventing the formation of a carbon star. The fact that dust-enshrouded carbon stars more luminous than $M_{bol} = -6$ mag are not entirely absent in the LMC means that HBB cannot be effective during the entire duration of the TP-AGB. HBB may shut off near the very end of the TP-AGB when mass loss has reduced the mass of the mantle to below a critical value needed to maintain the high pressure and temperature required for HBB to occur (Boothroyd & Sackmann 1992). Dredge-up of carbon by another thermal pulse may then cause the photospheric carbon-to-oxygen ratio to exceed unity (Frost et al. 1998; Marigo et al. 1998). With 3 out of 13 dust-enshrouded AGB stars between $M_{bol} = -6$ and -7 mag being carbon stars, this means that massive AGB stars (typically $M_{ZAMS} \sim 5 M_{\odot}$) experience about four to five thermal pulses during the dust-enshrouded phase. AGB stars with $M_{ZAMS} \sim 5 M_{\odot}$ have interpulse periods of $\sim 1 \times 10^4$ yr (Vassiliadis & Wood 1993), yielding lifetimes for these dust-enshrouded AGB stars of $\sim 5 \times 10^4$ yr.

4.2. Mass-loss rates

In Fig. 9 the mass-loss rates are plotted versus the bolometric magnitudes for the stars in our sample. Before discussing the implications for the mass loss in the AGB and RSG phases, two possible selection effects need to be addressed.

First, faint stars with high mass-loss rates may have escaped selection due to the difficulty to detect their faint, obscured near-IR counterpart. Indeed, the two carbon stars IRAS05289–6617 with $M_{bol} = -4.15$ mag and $\dot{M} = 4.1 \times 10^{-5} M_{\odot} \text{ yr}^{-1}$ and IRAS05568–6753 with $M_{bol} = -5.40$ mag and $\dot{M} = 5.5 \times 10^{-5} M_{\odot} \text{ yr}^{-1}$ were only included because in both cases the IRAS point source had been erroneously identified with an M-type field star. The K-band magnitude of their real near-IR counterparts is expected to be fainter than $K \sim 19$ mag, which is beyond any of the near-IR searches done so far. Hence more such heavily obscured, bolometrically faint stars are expected to exist (see also paper III and Loup et al. 1999). From the luminosity distributions (Fig. 8) these are expected to be carbon stars. A similarly obscured object (S13) was found in the Small Magellanic Cloud by Groenewegen & Blommaert (1998).

Second, stars with small IR excesses have been largely excluded from our sample. This may have resulted in

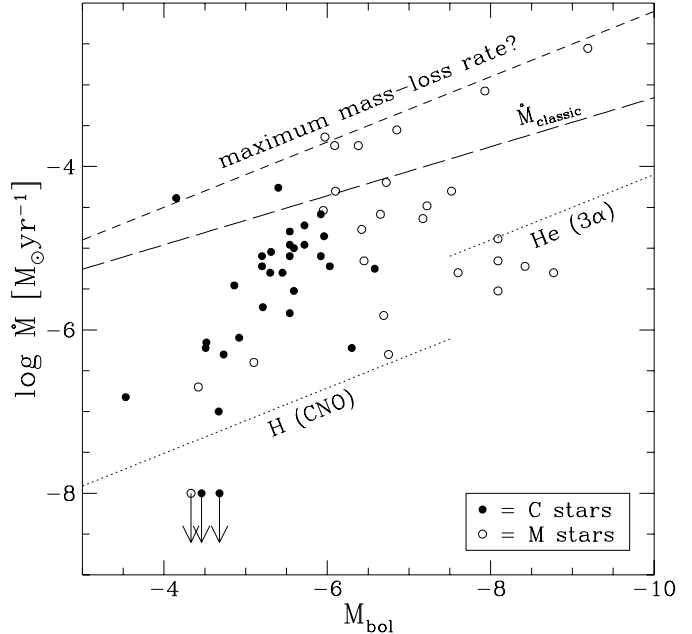


Fig. 9. Mass-loss rates versus bolometric luminosities for carbon and M-type stars. The distribution of stars suggests a maximum limit to \dot{M} which is proportional to L (short-dashed line) and higher than the classical limit $\dot{M}_{\text{classic}} = L(v_{\text{exp}}c)^{-1} \propto L^{0.75}$ (long-dashed line). The rates at which mass is burned by the CNO (AGB stars) and 3α (RSGs) cycles are also proportional to L (dotted lines).

the absence of stars with $\dot{M} \lesssim 10^{-7} M_{\odot} \text{ yr}^{-1}$ around $M_{bol} \sim -4$ mag to stars with $\dot{M} \lesssim 10^{-6} M_{\odot} \text{ yr}^{-1}$ around $M_{bol} \sim -9$ mag. It would be interesting to investigate whether this region in the \dot{M} versus M_{bol} diagram is in fact devoid of stars. Gail & Sedlmayr (1987) suggested that dynamical considerations exclude dust-driven winds with $\dot{M} \lesssim \text{few} \times 10^{-6} M_{\odot} \text{ yr}^{-1}$ (at $L \sim \text{few} \times 10^3 L_{\odot}$), which is reproduced in recent model calculations by Schröder et al. (1999). The values for \dot{M} that we find for faint stars of $L \sim \text{few} \times 10^3 L_{\odot}$ are more than an order of magnitude lower than the lower limit predicted by Gail & Sedlmayr (1987). These stars provide direct evidence for the existence of a wind-driving mechanism other than purely radiation pressure on dust.

On average mass-loss rates appear to be higher for the M-type stars than for the carbon stars in our sample, but this is a result of the higher luminosities of the M-type stars in our sample rather than the different chemistry per se (Fig. 9). The data suggest a maximum limit to the mass-loss rate, outlined by a (short-dashed) line of $\dot{M} \propto L$. There does not seem to be a distinction between the luminosity dependence of the maximum \dot{M} for AGB stars — be it carbon or M-type — and RSGs, despite their different masses and internal structure. The maximum \dot{M} is higher than the classical single-scattering limit $\dot{M}_{\text{classic}} = L(v_{\text{exp}}c)^{-1} \propto L^{0.75}$ (Jura 1984) by a factor ~ 2

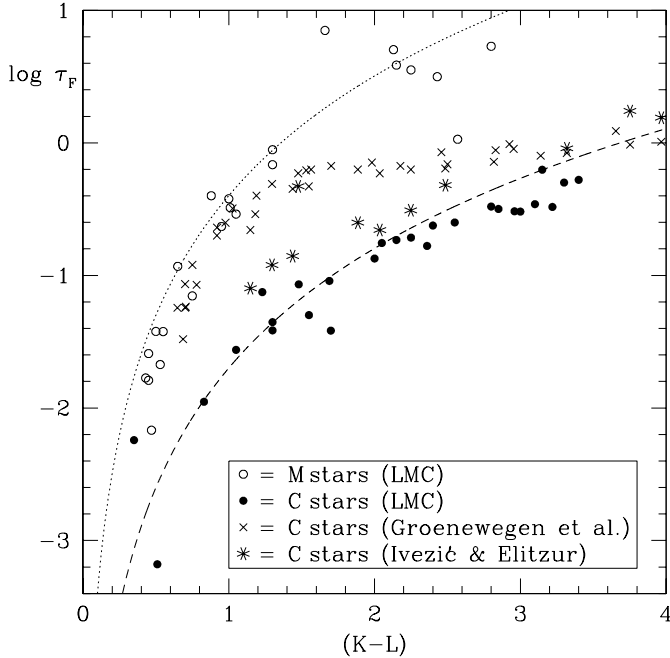


Fig. 10. Flux-weighted optical depth τ_F versus $(K - L)$ colour. The correlation for M-type stars in the LMC (open circles) is approximated by the dotted line, whereas the correlation for carbon stars in the LMC (solid circles) is approximated by the dashed line. Also plotted are galactic carbon stars, with τ_F values from Groenewegen et al. (1998) (crosses) and Ivezić & Elitzur (1995) (stars).

at $L = 10^3 L_\odot$ up to a factor ~ 10 at $L = 5 \times 10^5 L_\odot$. This is expected to happen when multiple scattering of photons in the dusty CSE becomes important (Gail & Sedlmayr 1986). The six M-type stars closest to the \dot{M} limit are indeed also the stars with the largest optical depth at $1 \mu\text{m}$ among the M-type stars, averaging $\tau_{\text{rad}}(1 \mu\text{m}) = 9 \pm 2$. The same is true for the two carbon stars near the \dot{M} limit, IRAS05289–6617 and IRAS05568–6753, that have the largest optical depth among the carbon stars, with $\tau_{\text{rad}}(1 \mu\text{m}) = 76$ and 56, respectively.

The factor $\dot{M}/\dot{M}_{\text{classic}}$ can be identified with the flux-weighted optical depth τ_F (cf. Ivezić & Elitzur 1995; Groenewegen et al. 1998, and references therein). In Fig. 10 the values of $\tau_F = \dot{M}/\dot{M}_{\text{classic}}$ for the M-type stars (open circles) and carbon stars (solid circles) in our ISO sample in the LMC are plotted against their $(K - L)$ colours. Not surprisingly, these two quantities are well correlated and can be reasonably well approximated by $\tau_F \sim 0.4 \times (K - L)^3$ for the M-type stars (dotted line) and $\tau_F \sim 0.02 \times (K - L)^3$ for the carbon stars (dashed line). From Fig. 10 it can be seen that multiple scattering already becomes important ($\tau_F \gtrsim 1$) for M-type stars with $(K - L) \gtrsim 1.5$ mag, whereas for carbon stars it only becomes important for $(K - L) \gtrsim 4$ mag. The fact that the two LMC carbon stars with $\tau_F > 1$ had not been identified in the near-IR is consistent with their expected $(K - L) \gg 4$

mag on the basis of Fig. 10. The galactic carbon stars from Groenewegen et al. (1998) are plotted for comparison (crosses). These are real flux-weighted optical depths, i.e. they were not calculated from the mass-loss rate, luminosity and expansion velocity. The flux-weighted optical depths of the galactic carbon stars from Ivezić & Elitzur (1995) are plotted too (stars). For both galactic samples we use the $(K - L)$ colours of the model fits from Groenewegen et al., after transformation onto the SAAO system (Carter 1990). The Ivezić & Elitzur values of τ_F are in better, but not exact, agreement with the carbon stars in the LMC. The reason for the discrepancy between the galactic carbon stars and the carbon stars in the LMC, and between the work of Groenewegen et al. and Ivezić & Elitzur is likely to be related to the different optical properties assumed for the dust by the various authors.

To appreciate the importance of the mass-loss rate for the evolution of a star, \dot{M} should be compared with the rate at which mass is consumed by nuclear burning, \dot{M}_{nuc} , and which determines the evolutionary timescale in the absence of severe mass loss. In AGB stars the energy is mainly produced by the CNO cycle in the H-burning shell, releasing $\sim 6.1 \times 10^{18}$ erg g $^{-1}$, whilst in RSGs the 3α cycle in the He-burning core is responsible for the stellar luminosity, releasing $\sim 5.9 \times 10^{17}$ erg g $^{-1}$ (Kippenhahn & Weigert 1990). The lines of \dot{M}_{nuc} are proportional to L (dotted in Fig. 9). All AGB stars in our sample with measurable mid-IR emission from circumstellar dust have $\dot{M} > \dot{M}_{\text{nuc}}$, and hence their AGB evolution will be terminated by the loss of the stellar mantle before the core can grow significantly. Indeed, the extreme AGB stars with $\tau_F > 1$ have lifetimes of only of the order of 10^4 yr, which is comparable to the interpulse timescale (Vassiliadis & Wood 1993). Most RSGs ($M_{\text{bol}} < -7.5$ mag), however, experience $\dot{M} \sim \dot{M}_{\text{nuc}}$. This means that they cannot lose a large fraction of their stellar mantles before presumably ending as supernovae. WOH G64 with $M_{\text{bol}} = -9.19$ mag and $\dot{M} = 2.8 \times 10^{-3} M_\odot \text{ yr}^{-1}$ and probably also IRAS04530–6916 with $M_{\text{bol}} = -7.93$ mag and $\dot{M} = 8.4 \times 10^{-4} M_\odot \text{ yr}^{-1}$ may be the only RSGs in our sample that have $\dot{M} \gg \dot{M}_{\text{nuc}}$. At such high mass-loss rates these two stars have lifetimes of only $\sim 2 \times 10^4$ yr.

The empty area in the $(M_{\text{bol}}, \dot{M})$ diagram between the two RSGs WOH G64 and IRAS04530–6916 with $\log \dot{M} = -2.6$ and -3.1 , respectively, and the six RSGs with about two orders of magnitude lower mass-loss rates is hard to explain in terms of selection effects and may therefore be a real gap in the \dot{M} distribution of RSGs. From these numbers we estimate that RSGs spend about 25% of their RSG lifetime in the intense mass-loss phase at $\dot{M} \sim 10^{-3} M_\odot \text{ yr}^{-1}$ and 75% in a moderate mass-loss phase at $\dot{M} \sim 10^{-5} M_\odot \text{ yr}^{-1}$. A similar gap of about an order of magnitude in \dot{M} may be present in the \dot{M} distribution of AGB stars, although for stars fainter than $M_{\text{bol}} \sim -6$ mag this is hard to prove due to the selection effects mentioned before. If true, however, this means

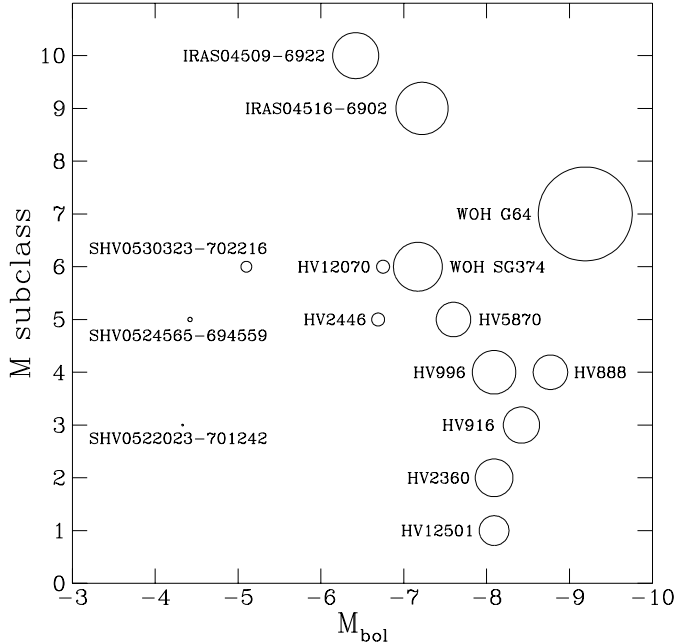


Fig. 11. Spectral subclasses versus bolometric luminosities for the M-type stars with known spectral type. The size of the symbol increases with larger \dot{M} . Stars of later spectral type (cooler T_{eff}) and higher luminosity have larger \dot{M} .

for the AGB stars that most ($\sim 80\%$) of the time on the TP-AGB is spent in relative quiescence, at high but not extraordinarily high \dot{M} , with only short phases of intense mass loss (see also Vassiliadis & Wood 1993). Such a “burst” may be episodic, or it may be the final shedding of the stellar mantle before the star leaves the AGB. According to recent evolutionary calculations by Schröder et al. (1998, 1999), which take into account the characteristics of dust-induced mass-loss from pulsating AGB stars, the duration of the high mass-loss phases strongly depends on the initial stellar mass.

The two brightest carbon stars in the sample, IRAS04496–6958 with $M_{\text{bol}} = -6.6$ and SHV0521050–690415 with $M_{\text{bol}} = -6.3$ mag have mass-loss rates that are significantly lower than the mass-loss rates of most of the oxygen-rich AGB stars at these high luminosities. We speculate that these stars may exhibit lower mass-loss rates following a (final) thermal pulse (Schröder et al. 1998, 1999) that converted them from oxygen-rich AGB stars into carbon stars after HBB could not be maintained anymore because the stellar mantles had been strongly diminished by mass loss on the TP-AGB. This strengthens the explanation of the silicate dust around IRAS04496–6958 being due to a final thermal pulse, as suggested by Trams et al. 1999a.

The process of dust formation is extremely sensitive to the temperature (Arndt et al. 1997), and (episodes of) increased mass-loss rates may therefore be related to lower T_{eff} of the stars. The spectral subclasses of the M-type

stars in our sample for which the spectral type is known are plotted versus their bolometric magnitudes (Fig. 11), with the size of the symbol increasing with larger \dot{M} . The strong luminosity dependence of \dot{M} is very prominent. However, there also seems to be a temperature dependence of \dot{M} : cooler stars, i.e. stars with larger subclasses, experience larger \dot{M} than warmer stars. Because the luminosity, effective temperature and surface gravity are inter-related (via the stellar radius) it is not yet clear to what extent the dependence of \dot{M} on L and T_{eff} reflects a dependence of \dot{M} on $\log g$.

5. Summary

We derived mass-loss rates and luminosities for a sample of dust-enshrouded oxygen- and carbon-rich AGB stars as well as a few optically bright AGB stars and red supergiants, all of which have been observed with ISO, using a radiation transfer code to model the spectral energy distributions at IR wavelengths.

The luminosity distribution of dust-enshrouded carbon stars peaks at $M_{\text{bol}} \sim -5.7$ mag, which is in between the peak of the luminosity distribution of optically bright carbon stars ($M_{\text{bol}} \sim -4.8$ mag) and the peak of the luminosity distribution of dust-enshrouded M-type AGB stars ($M_{\text{bol}} \sim -6.5$ mag). We interpret this as follows: stars with masses of ~ 2 to $4 M_{\odot}$ become dust-enshrouded carbon stars on the thermal pulsing AGB, whereas more massive AGB stars remain oxygen-rich as a result of Hot Bottom Burning. Optically bright carbon stars may still evolve in luminosity before becoming dust-enshrouded, or they may be associated with generally less massive stars (1 to $2 M_{\odot}$) than the stars that become dust-enshrouded carbon stars. The existence of a few luminous carbon stars may be explained by HBB switching off near the very tip of the AGB and the occurrence of a final thermal pulse thereafter.

Mass-loss rates of both AGB stars and RSGs are found to increase with increasing luminosity and decreasing effective temperature, and are typically $\dot{M} \sim 10^{-6}$ to $10^{-4} M_{\odot} \text{ yr}^{-1}$ on the TP-AGB and $\dot{M} \sim 10^{-5}$ to $10^{-3} M_{\odot} \text{ yr}^{-1}$ for RSGs. Mass-loss rates in some cases exceed the limit set by the rate at which the available photon momentum can be transferred onto the gas and dust by means of single scattering, providing evidence for multiple scattering to be effective in driving the outflow. Such intense mass loss only happens during distinct (possibly recurrent) phases in the evolution of AGB stars and RSGs that last typically 20 to 25% of the dust-enshrouded lifetime. It is only during these episodes of intensified mass loss that the mass-loss rate of RSGs exceeds the mass-consumption rate due to nuclear burning, whereas the mass-loss rate of dust-enshrouded AGB stars always exceeds the mass-consumption rate due to nuclear burning.

Acknowledgements. We would like to thank Dr. Carlos Lázaro for making his near-IR spectra of carbon stars available in elec-

tronic form, Prof.Dr. Teije de Jong and Jeroen Bouwman for valuable suggestions, the referee Dr. Jan Martin Winters for his excellent remarks that helped improve the presentation and discussion of the results, and Joana Oliveira for everything. We made use of the Astronomical Data Center, operated at NASA GSFC. A major part of this research was performed when JvL was at the University of Amsterdam, and supported by NWO Pionier Grant 600-78-333. AdK also acknowledges support from NWO Spinoza Grant 08-0 to E.P.J. van den Heuvel. JvL adds: Anjo, agora sou todo teu!

References

- Arndt T.U., Fleischer A.J., Sedlmayr E., 1997, *A&A* 327, 614
 Barnbaum C., Stone R.P.S., Keenan P.C., 1996, *ApJS* 105, 419
 Boothroyd A.I., Sackmann I.-J., 1992, *ApJ* 393, L21
 Bowen G.H., 1988, *ApJ* 329, 299
 Carter B.S., 1990, *MNRAS* 242, 1
 Costa E., Frogel J.A., 1996, *AJ* 112, 2607
 Feast M.W., 1996, *MNRAS* 278, 11
 Feast M.W., 1998, in: *New Views of the Magellanic Clouds*, eds. Y.-H. Chu, N.B. Suntzeff, J.E. Hesser, D.A. Bohlender. ASP Conf. Ser., p52
 Fluks M.A., Plez B., Thé P.S., de Winter D., Westerlund B.E., Steenman H.C., 1994, *A&AS* 105, 311
 Frost C.A., Cannon R.C., Lattanzio J.C., Wood P.R., Forestini M., 1998, *A&A* 332, L17
 Gail H.-P., Sedlmayr E., 1986, *A&A* 161, 201
 Gail H.-P., Sedlmayr E., 1987, *A&A* 177, 186
 Goldreich P., Scoville N.Z., 1976, *ApJ* 205, 144
 Groenewegen M.A.T., Blommaert J.A.D.L., 1998, *A&A* 332, 25
 Groenewegen M.A.T., de Jong T., 1993, *A&A* 267, 410
 Groenewegen M.A.T., Whitelock P.A., Smith C.H., Ker-schbaum F., 1998, *MNRAS* 293, 18
 Habing H.J., Tignon J., Tielens A.G.G.M., 1994, *A&A* 286, 523
 Hron J., Loidl R., Höfner S., et al., 1998, *A&A* 335, L69
 Iben I., 1981, *ApJ* 246, 278
 Iben I., Renzini A., 1983, *ARA&A* 21,271
 Ivezić Ž., Elitzur M., 1995, *ApJ* 445, 415
 Jäger C., Molster F.J., Dorschner J., et al., 1998, *A&A* 339, 904
 Jura M., 1984, *ApJ* 282, 200
 Kippenhahn R., Weigert A., 1990, *Stellar Structure and Evolution*. Springer, Berlin, p166
 Laor A., Draine B.T., 1993, *ApJ* 402, 441
 Lázaro C., Hammersley P.L., Clegg R.E.S., et al., 1994, *MNRAS* 269, 365
 Loup C., Zijlstra A.A., Waters L.B.F.M., Groenewegen M.A.T., 1997, *A&AS* 125, 419 (paper I)
 Loup C., Josselin E., Cioni M.-R., et al., 1999, in: *Asymptotic Giant Branch Stars*, eds. C. Waelkens, T. Leberdre, A. Lèbre. ASP Conf. Ser., p561
 Marigo P., Bressan A., Chiosi C., 1998, *A&A* 331, 564
 Molster F.J., Waters L.B.F.M., Trams N.R., van Winckel H., Decin L., van Loon J.Th., Jäger C., Henning Th., Käuff H.-U., de Koter A., Bouwman J., 1999, *A&A* in press
 Preibisch Th., Ossenkopf V., Yorke H.W., Henning Th., 1993, *A&A* 279, L33
 Reid N., Tinney C., Mould J., 1990, *ApJ* 348, 98
 Schröder K.-P., Winters J.M., Arndt T.U., Sedlmayr E., 1998, *A&A* 335, L9
 Schröder K.-P., Winters J.M., Sedlmayr E., 1999, *A&A* 349, 898
 Schwering P.B.W., Israel F.P., 1990, *A catalog of IRAS sources in the Magellanic Clouds*. Kluwer, Dordrecht
 Trams N.R., van Loon J.Th., Zijlstra A.A., et al., 1999a, *A&A* 344, L17
 Trams N.R., van Loon J.Th., Waters L.B.F.M., et al., 1999b, *A&A* 346, 843
 van Loon J.Th., 1999, submitted to *A&A Main Journal*
 van Loon J.Th., Molster F.J., van Winckel H., Waters L.B.F.M., 1999b, *A&A* in press
 van Loon J.Th., Zijlstra A.A., Whitelock P.A., et al., 1997, *A&A* 325, 585 (paper III)
 van Loon J.Th., Zijlstra A.A., Whitelock P.A.W., et al., 1998, *A&A* 329, 169 (paper IV)
 van Loon J.Th., Zijlstra A.A., Groenewegen M.A.T., 1999a, *A&A* 346, 805
 Vassiliadis E., Wood P.R., 1993, *ApJ* 413, 641
 Walker A.R., 1999, in: *Post Hipparcos Cosmic Candles*, eds. F. Caputo & A. Heck. Kluwer, Dordrecht, p125
 Waters L.B.F.M., Beintema D.A., Cami J., et al., 1999, in: *The Universe as seen by ISO*, eds. P. Cox and M.F. Kessler. ESA SP-427, in press
 Weigelt G., Balega Y., Blöcker T., et al., 1998, *A&A* 333, L51
 Wickramasinghe N.C., Donn B.D., Stecher T.P., 1966, *ApJ* 146, 590
 Wood P.R., 1998, *A&A* 338, 592
 Wood P.R., Bessell M.S., Fox M.W., 1983, *ApJ* 272, 99
 Wood P.R., Bessell M.S., Whiteoak J.B., 1986, *ApJ* 306, L81
 Wood P.R., Whiteoak J.B., Hughes S.M.G., et al., 1992, *ApJ* 397, 552
 Zijlstra A.A., Loup C., Waters L.B.F.M., et al., 1996, *MNRAS* 279, 32 (paper II)